Supplementary Information for

Tuning optical properties of densified silica glass via high pressure and ultrafast laser excitation

Misora Tsubone[1], Yasuhiko Shimotsuma[1]*, Yoshio Kono[2], Sho Kakizawa[3], Hiroki Yamada[3], Keita Kobayashi[4], Masahiro Shimizu[1] & Kiyotaka Miura[1]

[1] Department of Material Chemistry, Kyoto University, Kyoto 615-8510, Japan

[2] Department of Physics and Astronomy, Kwansei Gakuin University, Sanda 669-1330, Japan

[3] Japan Synchrotron Radiation Research Institute, Hyogo 679-5198, Japan

[4] CCSE, Japan Atomic Energy Agency, Kashiwa, Chiba 277-0871, Japan.

* Corresponding author. Email: shimotsuma.yasuhiko.3m@kyoto-u.ac.jp

This Supplementary Information includes:

1. Calibration curve for conversion from Raman main band position to fictive temperature

Previous studies have demonstrated that the position of the Raman main band shifts monotonically with increasing fictive temperature (T_f) (1-4). To establish a calibration curve for converting the Raman main band position to T_f, silica glass samples (VIOSIL-LSX, Shin-Etsu Chemical Co.) were annealed at various temperatures ranging from 1273K to 1673K for a sufficient duration to achieve structural relaxation (τ) (5). Each sample was placed on a thin Pt film deposited on an alumina plate and annealed in a furnace. After annealing, the samples were rapidly quenched by immersion in distilled water. The annealing conditions are summarized in Table S1. Raman spectra near the main band were fitted using a Gaussian function to determine the peak position (ν). Fig. S1 presents the observed Raman spectra of samples annealed at various conditions and the resulting calibration curve for fictive temperature (T_f).

Table S1 | Annealing conditions

T_f [K]	τ [sec]	annealing time
1273	4.3×10^4	3 days
1373	1.6×10^3	3 hours
1473	88	1 hour
1573	7.2	30 minutes
1673	0.8	30 minutes

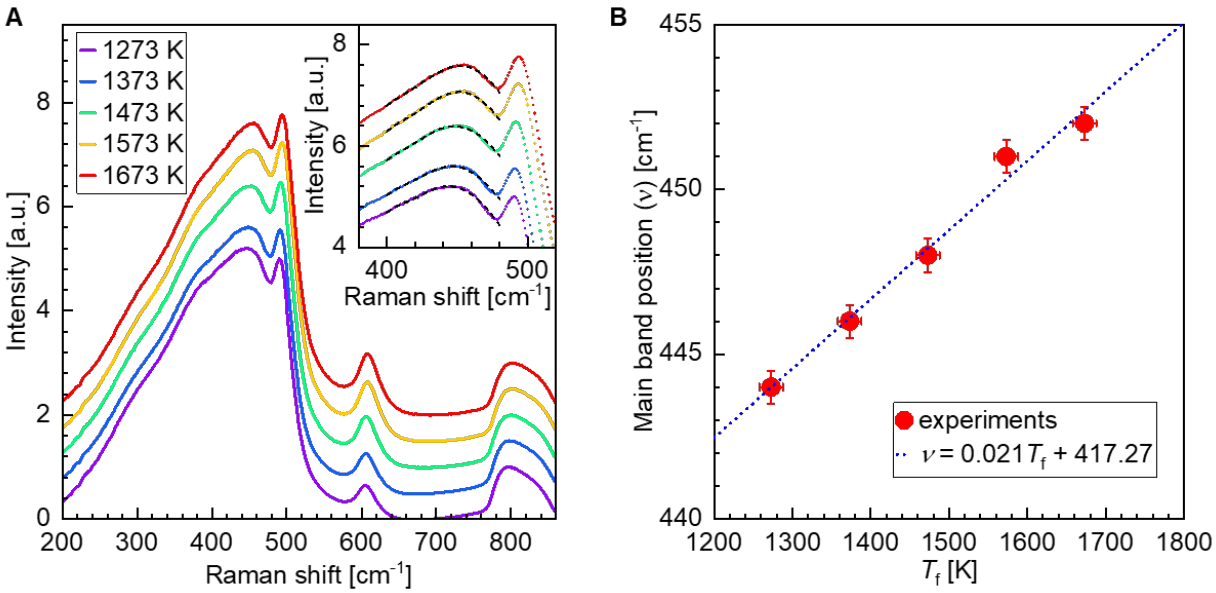

Figure S1 | Calibration curve for fictive temperature from Raman main band position. (**A**) Raman spectra of silica glass samples annealed under the conditions listed in Table S1. Spectra are vertically offset for clarity. The inset shows a magnified view near the Raman main band, with dashed curves indicating Gaussian fits used to determine the peak position (ν). (**B**) Plot of the Raman main band position as a function of fictive temperature, along with the fitted calibration curve. The estimated error bars for ν and T_f are 0.5 cm^{-1} and 15 °C, respectively.

2. Raman D1 and D2 band behavior

Fig. S2 presents the intensity and position of the Raman D1 and D2 bands as functions of applied pressure for glass samples subjected to HPHT treatments. Similar plots are shown for samples that underwent combined HPHT treatment and FLDW, with the laser pulse energy as a variable. Raman D1 and D2 band intensities were determined by subtracting the Raman main band as the broad background. Fig. S3 shows confocal Raman spectra of silica glass after FLDW, HPHT treatment, and their sequential combinations. The responses of the Raman main band, D1 band, and D2 band under HPHT treatment and FLDW are summarized in Table S2.

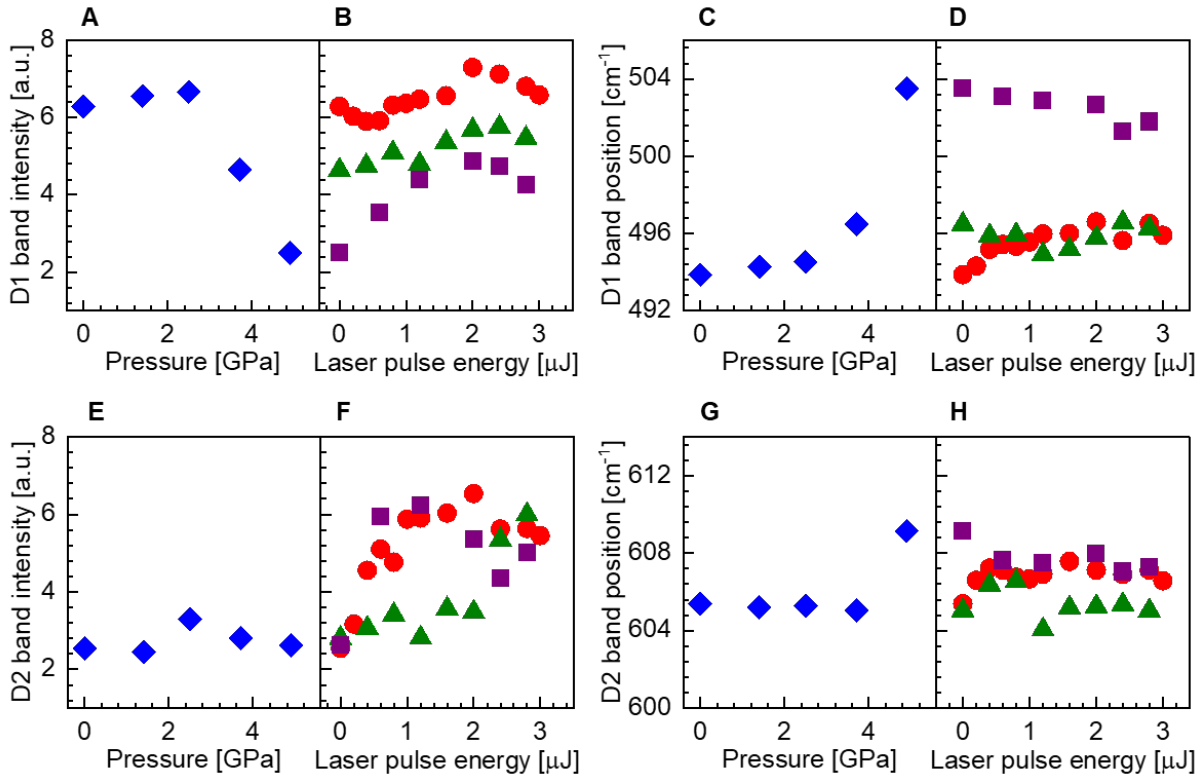

Figure S2 | Variation of Raman D1 and D2 bands induced by HPHT treatment and FLDW. Plots of Raman D1 and D2 band intensities and positions as a function of applied pressure and laser pulse energy. (**A**, **E**) D1 and D2 band intensities as a function of applied pressure for glass samples subjected to HPHT treatments, (**C**, **G**) D1 and D2 band positions as a function of applied pressure. (**B**, **F**) D1 and D2 band intensities as a function of laser pulse energy for glass samples subjected to combined HPHT treatment and FLDW. (**D**, **H**) D1 and D2 band positions as a function of laser pulse energy. Red circles, green triangles, and purple squares indicate results for samples with no pressure, 3.7 GPa, and 4.9 GPa high pressure treatments, respectively.

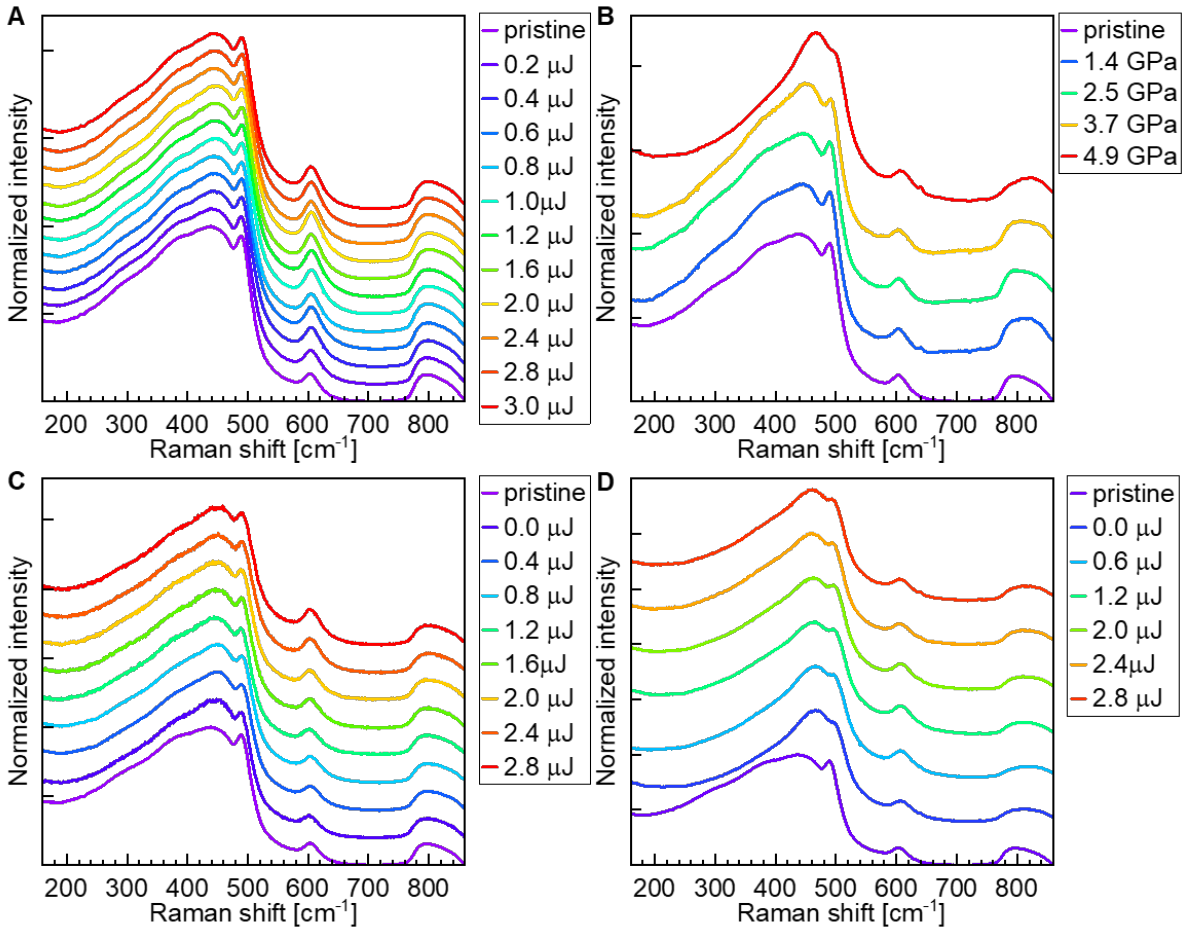

Figure S3 | Confocal Raman spectra of silica glass under various treatments. Confocal Raman spectra of silica glass modified by FLDW, HPHT treatments, and their sequential combinations. Femtosecond laser pulses (2.5×10^6 pulses) were irradiated with varying pulse energies. HPHT treatments were conducted at different pressures for 1 hour at 673 K. (**A**) FLDW, (**B**) HPHT treatment, (**C**) HPHT treatment at 3.7 GPa followed by FLDW, and (**D**) HPHT treatment at 4.9 GPa followed by FLDW.

Table S2 | Summary of Raman band behaviors under HPHT treatment and FLDW

Raman band	Peak parameter	HPHT	FLDW	HPHT (3.7 GPa) → FLDW	HPHT (4.9 GPa) → FLDW
main	Position	higher	higher	slightly increase	decrease
	Width	narrower	largely unchanged	largely unchanged	largely unchanged
D1	Intensity	decrease	increase	slightly increase	increase
	Position	higher	higher	largely unchanged	slightly lower
D2	Intensity	largely unchanged	increase	increase	increase
	Position	higher	higher	largely unchanged	slightly lower

3. Experimental X-ray pair-distribution function g(r) for silica glass

Fig. S4 presents the X-ray pair-distribution function g(r) for silica glass obtained by Fourier transforming the structure factors in Fig. 5 and Fig. 6.

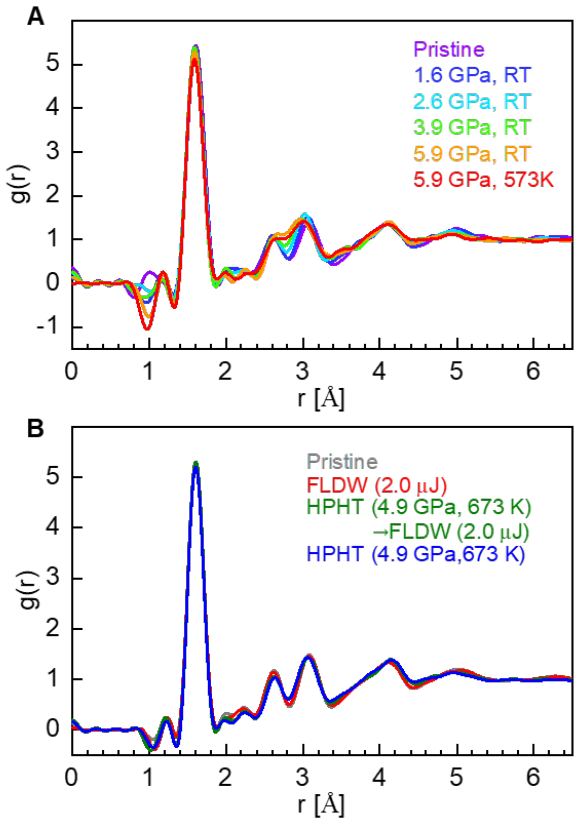

Figure S4 | Experimental X-ray pair-distribution function g(r) for silica glass. The data sets were obtained by Fourier transforming the structure factors in (**A**) Fig. 5 and (**B**) Fig. 6.

4. Femtosecond laser-irradiated samples for high-energy X-ray diffraction measurements

Large-volume laser-processed glass samples were prepared for high-energy X-ray diffraction measurements. Details of the fabricated structures are presented in Fig. S5. Based on the observed modification geometry, the laser-processed region was estimated to occupy approximately 17% of the total glass sample volume.

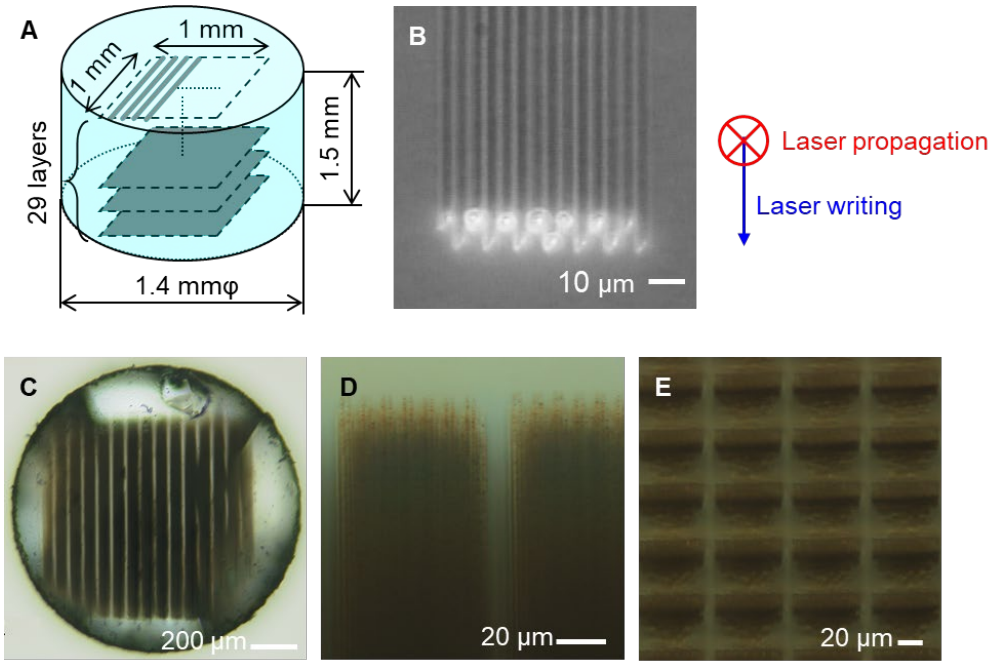

Figure S5 | Fabricated large-volume laser-processed glass samples. (**A**) Schematic illustration of the large-volume laser-processed glass sample, (**B**) Photograph of a typical femtosecond laser-processed region fabricated using simultaneous 14-point irradiation, (**C**) Optical microscope image of the laser-processed sample viewed from the top, (**D**) Enlarged view of the region shown in (**C**), (**E**) Optical microscope image of the processed sample viewed from the side.

5. Parameters associated with the Q_1 peak in S(Q) under various pressure conditions

Fig. S6 presents the parameters associated with the Q_1 peak in the structure factor S(Q) of silica glass under various pressure conditions at room temperature. The peak position, height, and width were determined from Lorentzian fits. The Q_1 peak, ranging from 0.4 Å^{-1} to 2.6 Å^{-1}, was fitted using the following Lorentzian function with a linear background.

$$y = \frac{ad}{\pi}\left\{\frac{1}{(x-Q)^2 + d^2}\right\} + bx + c$$

where a, b, c, d, and Q are the fitting parameters.

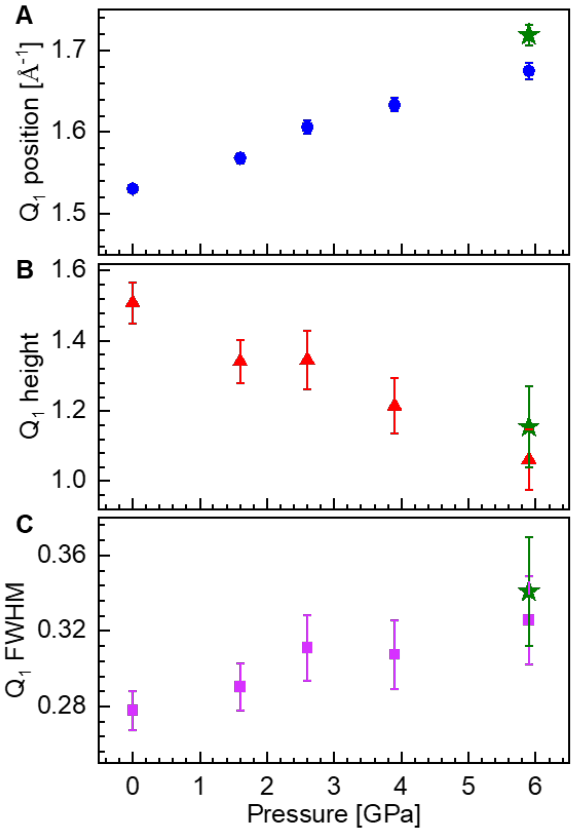

Figure S6 | Q_1 peak parameters of silica glass under various pressure conditions at room temperature. Parameters associated with the Q_1 peak in the structure factor S(Q) of silica glass under various pressure conditions at room temperature. (**A**) Peak position, (**B**) Peak height, and (**C**) Peak width, all determined by Lorentzian fitting. The green star symbol indicates the results obtained at 5.9 GPa under 573 K.

6. Temperature dependence of the X-ray structure factor S(Q)

Fig. S7 presents the structure factor S(Q) of silica glass obtained from in-situ synchrotron X-ray diffraction measurements conducted at various temperatures under ambient pressure. The parameters associated with the Q_1 peak in S(Q) under various temperature conditions are also shown in Fig. S7. Our observations indicate that the parameters of the Q_1 peak remained nearly constant across the different temperatures examined.

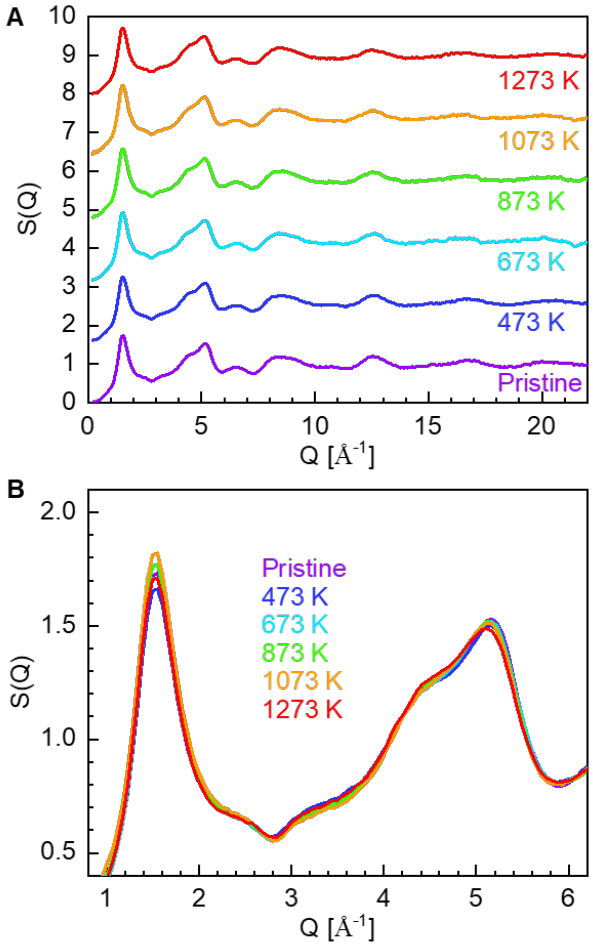

Figure S7 | Temperature dependence of structure factor S(Q). (**A**) Structure factor S(Q) of silica glass obtained from in-situ synchrotron X-ray diffraction measurements at various temperatures under ambient pressure. S(Q) curves are vertically offset by +0.8 for clarity. (**B**) Enlarged view of the experimentally observed S(Q) in the Q range between 0.8 and 6.2 Å^{-1}, displayed without a vertical offset.

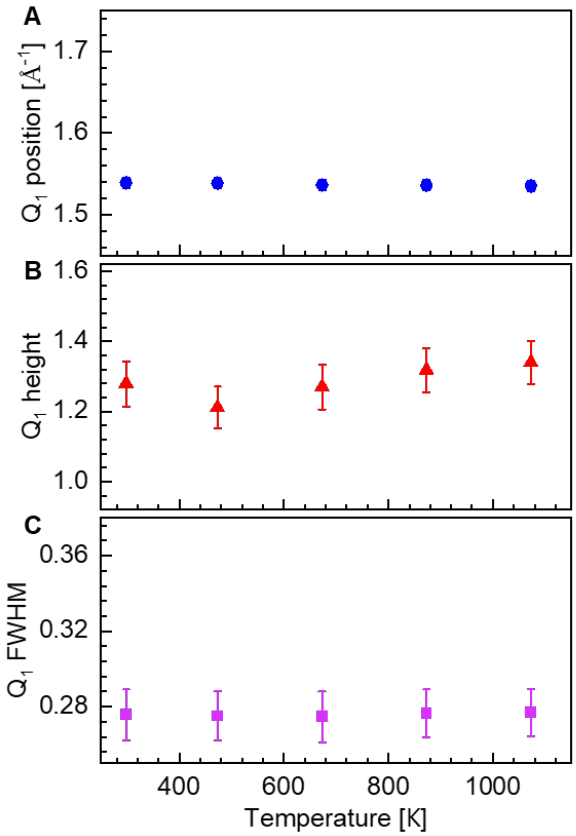

Figure S8 | Temperature dependence of Q_1 peak parameters in structure factor S(Q). Parameters associated with the Q_1 peak in S(Q) of silica glass under various temperatures. (**A**) Peak position, (**B**) Peak height, and (**C**) Peak width, all determined by Lorentzian fitting.

7. Parameters associated with the Q_1 peak in S(Q) under various treatments

Fig. S9 presents parameters associated with the Q_1 peak in S(Q) of silica glass subjected to high pressure treatment, laser irradiation, and their sequential combination (high pressure treatment followed by laser irradiation). The peak position, peak height, and peak width were determined by Lorentzian fitting.

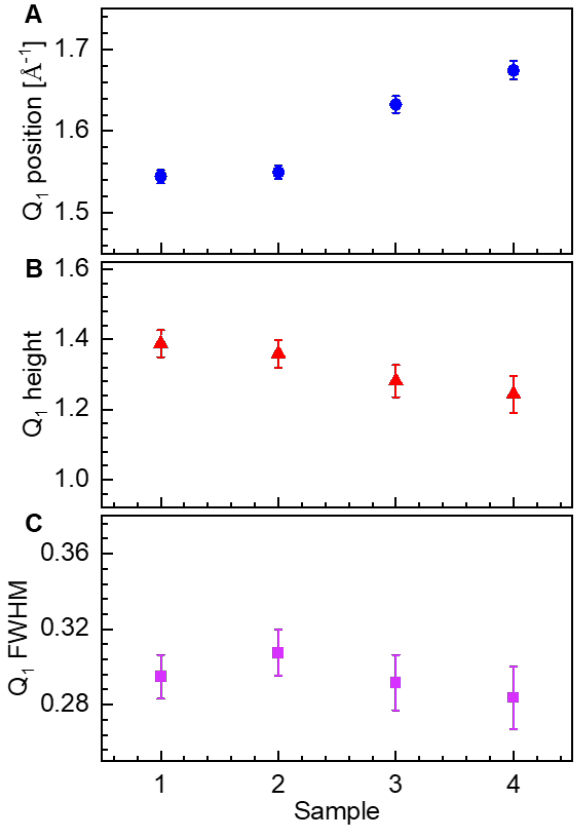

Figure S9 | Q_1 Peak Parameters of silica glass under various treatments. Parameters associated with the Q_1 peak in S(Q) of silica glass subjected to HPHT treatment, FLDW, and their sequential combinations (HPHT treatment followed by FLDW). (**A**) Peak position, (**B**) Peak height, and (**C**) Peak width, all determined by Lorentzian fitting. The horizontal axis corresponds to the sample numbers presented in Fig. 6. **1**. Pristine glass, **2**. FLDW glass (2.0 μJ, 2.5×10^6 pulses), **3**. HPHT (4.9 GPa, 673 K) followed by FLDW (2.0 μJ, 2.5×10^6 pulses), **4**. HPHT glass (4.9 GPa, 673 K).

8. Machine-learning molecular dynamics simulation

Machine learning molecular dynamics simulations were performed to investigate the structural changes in silica glass subjected to high-pressure treatment and laser irradiation. The MD simulations were conducted using the LAMMPS code (6) with a machine learning potential for silica developed in reference (7). Initially, we used a relatively small system (1,728 atoms) to explore the conditions for creating a high-density glass structure in silico, aiming to reproduce the density of experimentally obtained silica glass. The pristine glass structure was generated using the melt-quenching method, cooling from 3500 K to 300 K at a rate of 0.5 K/ps under NPT simulations. The density of the simulated pristine glass was 2.238 g/cm^3. The high-density glass was prepared by compressing the pristine glass at elevated temperature for 100 ps of simulation time, followed by cooling to 300 K at a rate of 0.5 K/ps. Fig. S10 presents the density and X-ray structure factor of high-pressure-treated silica glass containing 1728 atoms in reference (7). The high-density glass prepared at 1500 K and 10 GPa exhibited both a density and structure factor in close agreement with our experimental data. Therefore, the same high-pressure and high-temperature conditions were applied to a larger simulation system containing 13,824 atoms. The resulting density of this simulated high-density silica glass was 2.434 g/cm^3. These two distinct glass structures, pristine glass (PG) and high-density glass (HDG), were used in the subsequent simulations.

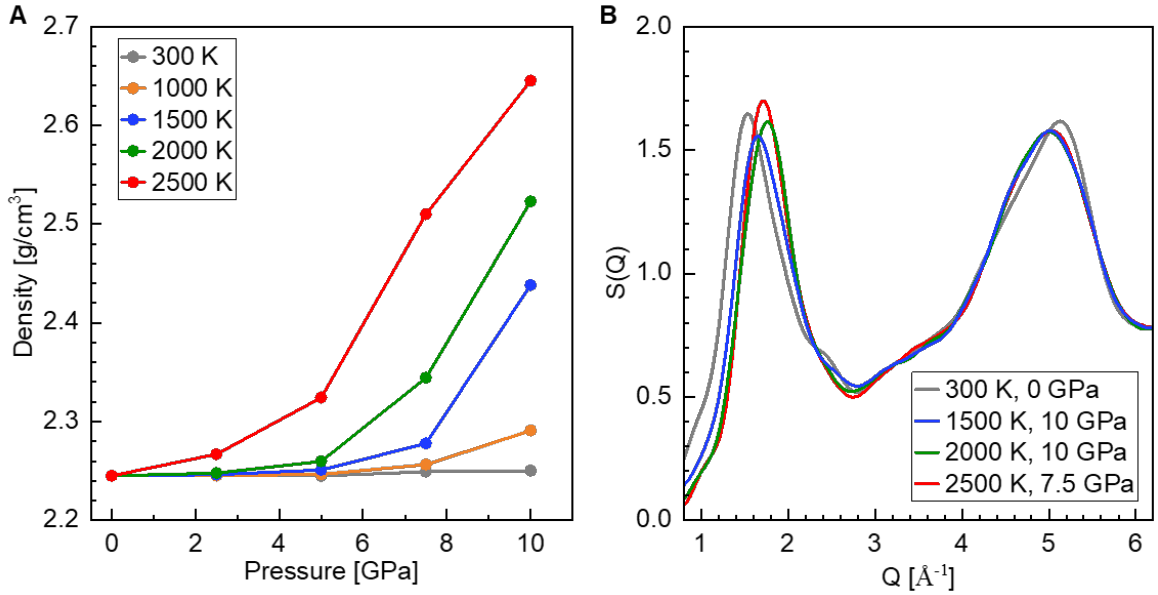

Figure S10 | Density and X-ray structure factor of simulated silica glass models under various pressure and temperature conditions. (**A**) Simulated density of silica glass compressed under various pressures (0, 2.5, 5.0, 7.5, and 10 GPa) and temperatures (300 K, 1000 K, 1500 K, 2000 K, and 2500 K). (**B**) X-ray total structure factor S(Q) of simulated pristine and high-density silica glass models. High-density glass structures compressed at 1500 K-10 GPa (2.438 g/cm^3), 2000 K-10 GPa (2.523 g/cm^3), and 2500 K-7.5 GPa (2.510 g/cm^3) were selected, as their simulated densities closely approximate the experimentally observed density of high-pressure-treated silica glass (2.46 g/cm^3).

Ultrashort pulse lasers can induce nonlinear ionization processes, such as multiphoton ionization and tunneling ionization, which lead to the breaking of atomic bonds. These processes represent strongly non-equilibrium phenomena, making it challenging to fully reproduce the underlying physics using MD simulations. However, Si-O bond dissociation at high temperatures is considered to partially mimic the bond-breaking induced by ultrashort pulse laser irradiation. In this study, laser irradiation was modeled by locally heating a part of the glass structure to a high temperature, followed by rapid cooling. We first performed NVT simulations in which a spherical region corresponding to 17% of the total volume of the silica glass structure was locally heated to 4000, 4500, and 5000 K for 10 ps. During this process, the motions of the silicon and oxygen atoms in the remaining 83% of the structure were completely frozen. Immediately after local heating, the system was cooled to 300 K using NPT simulations. This local heating condition is referred to as "LH", while the case without local heating is denoted as "noLH". Corresponding to the main glass samples in the experiment, [I] pristine glass, [II] laser-irradiated glass, [III] high-pressure-treated glass followed by laser irradiation, and [IV] high-pressure treatment, MD simulations were carried out for: [I] pristine glass (PG/noLH), [II] local heating of pristine glass (PG/LH), [III] local heating of high-density glass (HDG/LH), and [IV] high-density glass (HDG/noLH), respectively.

Fig. S11 shows the first peak of the simulated X-ray structure factor for (A) pristine glass (PG) and (B) high-density glass (HDG) under different local heating temperatures. For locally heated pristine glass (PG/LH), the intensity of the first peak decreases with increasing local heating temperature. In contrast, for locally heated high-density glass (HDG/LH), a slight shift of the first peak toward lower Q is observed at 4000 K, along with a small increase in peak height, consistent with the experimental trends. Within the scope of the present local-heating-based model, the structure factors of PG/LH at 5000 K and HDG/LH at 4000 K qualitatively reproduce the X-ray structure factors of laser-irradiated pristine glass and laser-irradiated high-pressure-treated glass, respectively (see Fig. 6 and 7). These results suggest that the structural modifications induced by laser irradiation in both pristine and high-pressure-treated glass are reasonably captured by the local heating simulations at 5000 K and 4000 K, respectively.

Fig. S12 shows the first peaks of the partial radial distribution functions (RDFs) and partial structure factors from simulations of PG/noLH, PG/LH@5000 K, HDG/LH@4000 K, and HDG/noLH. Among the RDFs (Fig. S12 A-C), the Si-Si pair exhibits the most pronounced change in the position and shape of its first peak. Additionally, in the partial structure factors, the Si–Si contribution exhibits more significant variation, particularly around the Q_3 peak (4 ~5 $Å^{-1}$). The change in the shape of the Q_3 peak is influenced not only by contributions from Si-O and O-O atomic pair correlations but also by the Si-Si correlation, indicating variations in the Si-O-Si bond angle, consistent with Raman spectral observations (Fig. S2 and S3).

The O-Si-O bond angle distributions from simulations of these glasses are shown in Fig. S13. This bond angle distribution becomes slightly broader in locally heated and high-density silica glasses compared to the pristine glass, but the peak position remains around 109°.

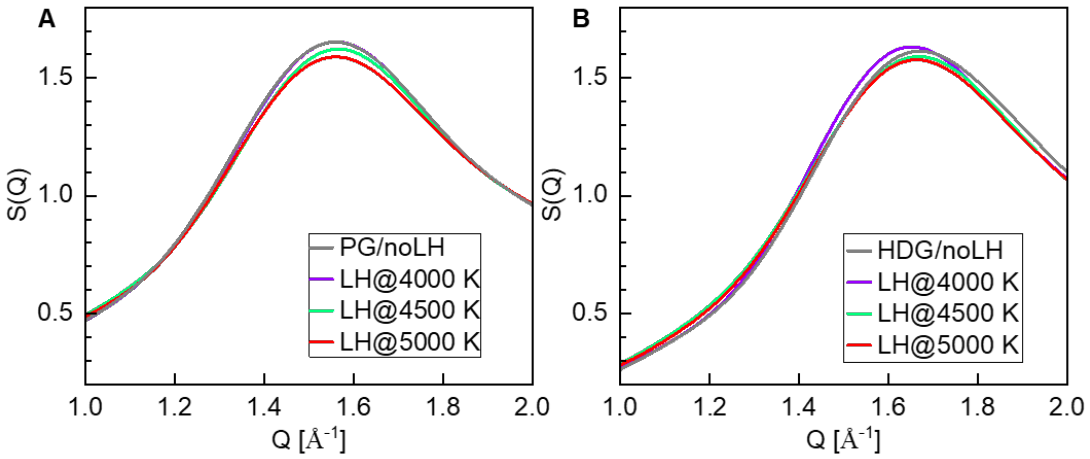

Figure S11 | First peak of the simulated X-ray structure factor under local heating. First peak of the simulated X-ray structure factor for (**A**) pristine glass (PG) and (**B**) high-density glass (HDG) under different local heating conditions.

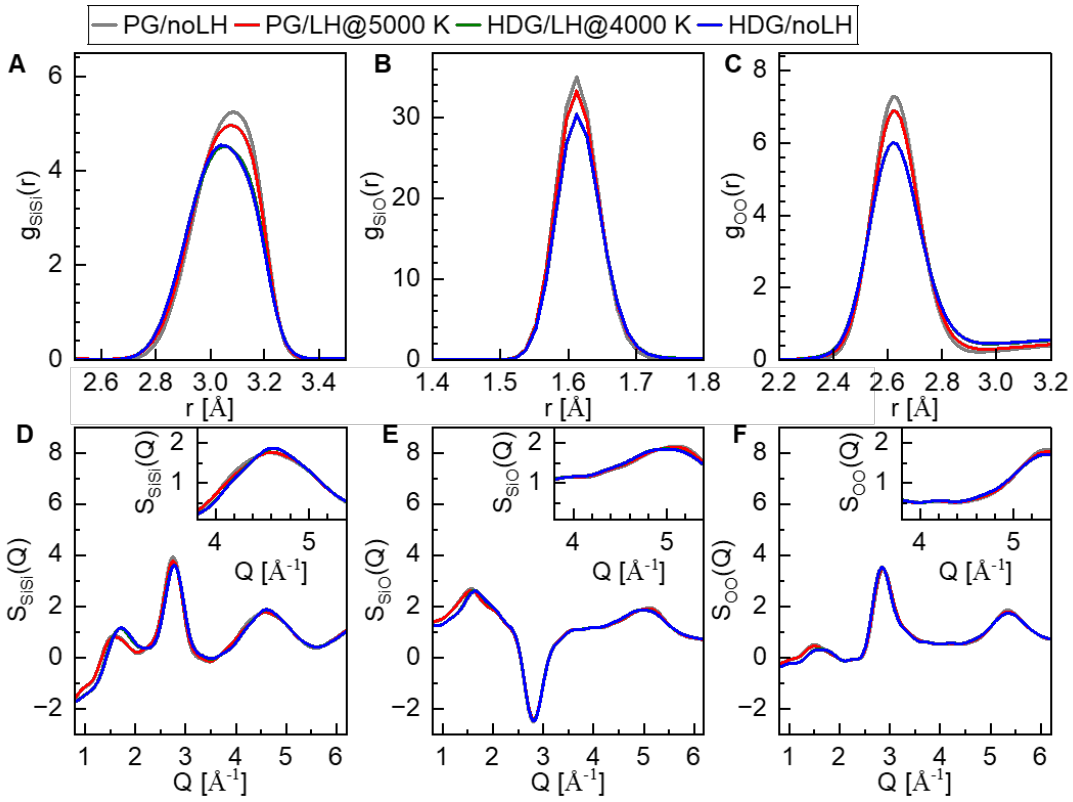

Figure S12 | Partial radial distribution functions and partial structure factors. First peaks of the partial radial distribution functions and the partial structure factors for (**A**, **D**) Si-Si, (**B**, **E**) Si-O, and (**C**, **F**) O-O atom pairs. Panels (**A**-**C**) show the partial radial distribution functions g(r), while panels (**D**-**F**) display the corresponding partial structure factors S(Q). Insets in (**D**-**F**) present enlarged view of each S(Q) around the Q_3 peak (4 ~ 5 Å^{-1}).

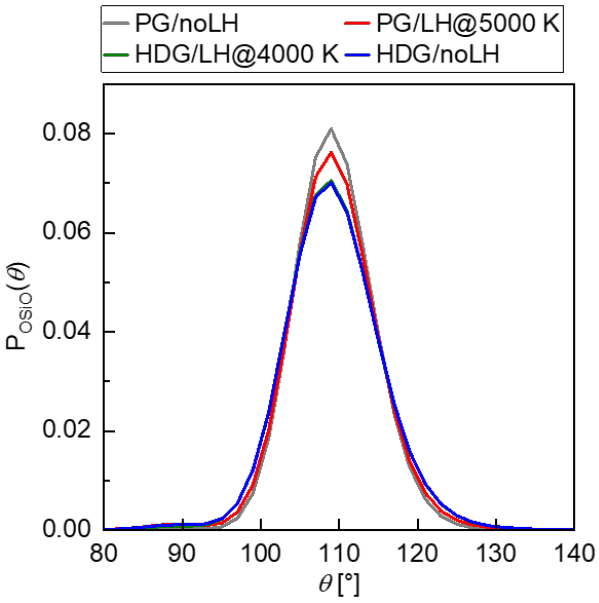

Figure S13 | bond angle distributions of O-Si-O. The bond angle distributions of O-Si-O obtained from simulations of PG/noLH, PG/LH@5000 K, HDG/LH@4000 K, and HDG/noLH.

Fig. S14 shows the ring-size distributions around silicon atoms, calculated using shortest-path analysis via a depth-first search algorithm. As shown in Fig. S14 A, high-density glass (HDG/noLH) tends to form larger rings, particularly 8- and 9-membered ones, compared to pristine glass (PG/noLH). Upon local heating (PG/LH@5000 K and HDG/LH@4000 K), the populations of both small (2- to 4-membered) and large (7- to 10-membered) rings slightly increase as well (Fig. S14 B), indicating that local heating promotes structural disorder of the glass network. This trend becomes more pronounced when focusing on atoms within the locally heated region (Fig. S14 C and D). Notably, the locally heated region of PG exhibits a significant rise in two-membered rings, defect structures typically associated with edge-sharing SiO_4 tetrahedra. The formation of such edge-sharing SiO_4 tetrahedra at high temperatures implies the generation of non-bridging oxygen atoms within the glass network. These results are consistent with the luminescence behavior of non-bridging oxygen atoms induced by the laser-irradiated silica glass.

Fig. S15 shows the density changes of pristine glass (PG) and high-density glass (HDG) induced by local heating. Upon local heating, the density of PG slightly increases, whereas that of HDG slightly decreases. These trends are consistent with experimental observations: the densification of laser-irradiated pristine glass (Fig. 1) and the shift of the Q_1 peak toward lower Q in high-pressure-treated glass by laser irradiation (Fig. 6 and S9).

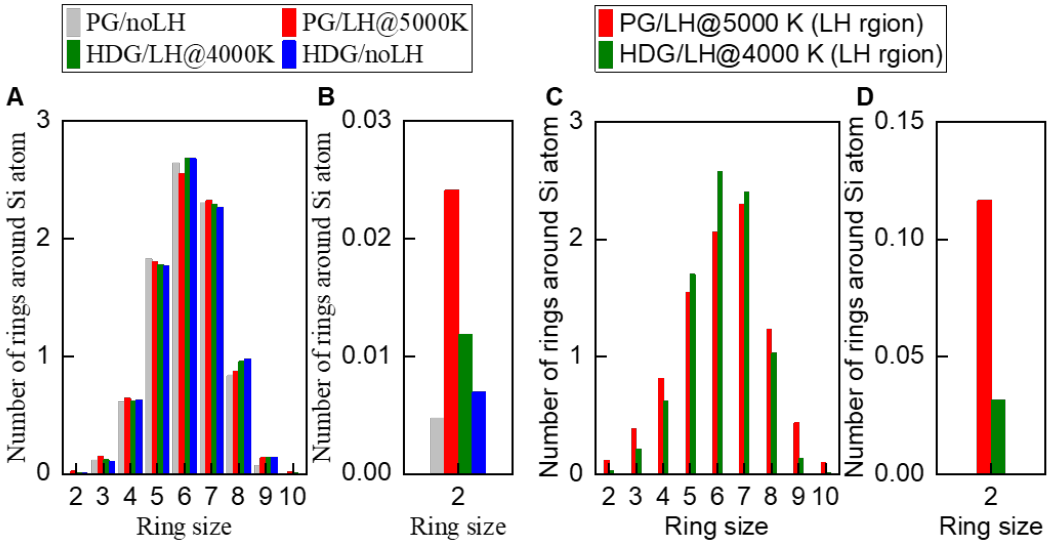

Figure S14 | Ring-size distribution around silicon atoms in simulated glass structures. Ring-size distribution around silicon atoms in simulated silica glass structures: PG/noLH, PG/LH@5000 K, HDG/LH@4000 K, and HDG/noLH. (**A**) and (**B**) present the ring-size distribution around silicon atoms across the entire simulation region. (**C**) and (**D**) show the ring-size distribution restricted to silicon atoms within the locally heated region. (**B**) and (**D**) focus exclusively on two-membered rings.

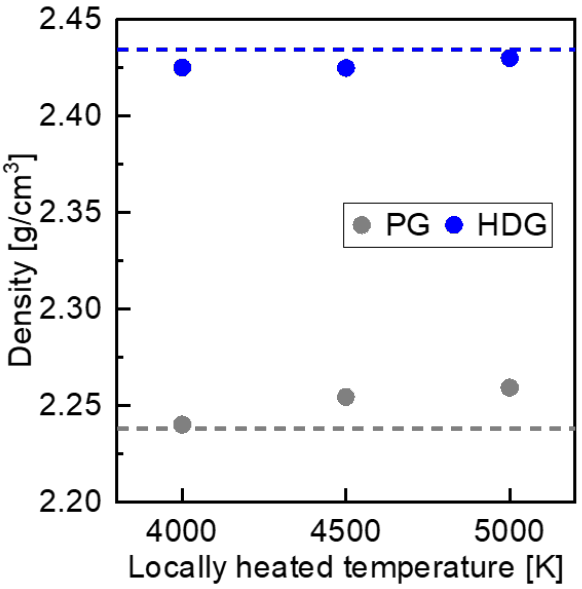

Figure S15 | Effect of local heating on the density of pristine and high-density silica glass. Effect of local heating on the density of pristine glass (PG) and high-density glass (HDG). Dotted blue and gray lines indicate the densities of PG and HDG without local heating, respectively.

9. Vibrational density of state (VDOS) calculated by Machine-learning MD simulation

To further investigate the changes in the Raman bands induced by FLDW and HPHT treatments, we simulated the vibrational density of states (VDOS) using machine-learning MD. In MD simulations, the total VDOS can be expressed as the sum of the atomic VDOS $g_i(\omega)$:

$$g(\omega) = \sum_{i}^{N} g_i(\omega).$$

The atomic-VDOS $g_i(\omega)$ represents the VDOS of atom i and was calculated from the velocity–velocity correlation function as

$$g_i(\omega) = \frac{2m_i}{3Nk_BT}\int_0^{t_{\max}-\tau_{\max}} dt \int_0^{\tau_{\max}} d\tau \boldsymbol{v}_i(t+\tau)\cdot \boldsymbol{v}_i(t)\cos(\omega\tau),$$

where m_i is the mass of atom i, N is the total number of atoms, k_B is the Boltzmann constant, T is the temperature, and $\mathbf{v}_i(t)$ is the velocity of atom i at time t. $t_{\max}$ denotes the total simulation time, and $\tau_{\max}$ is the maximum correlation time used in the integration. We performed NVE simulations for the PG/noLH, PG/LH@5000 K, HDG/LH@4000 K, and HDG/noLH structures. The total simulation time $t_{\max}$ was 300 ps and the maximum correlation time $\tau_{\max}$ was 20 ps.

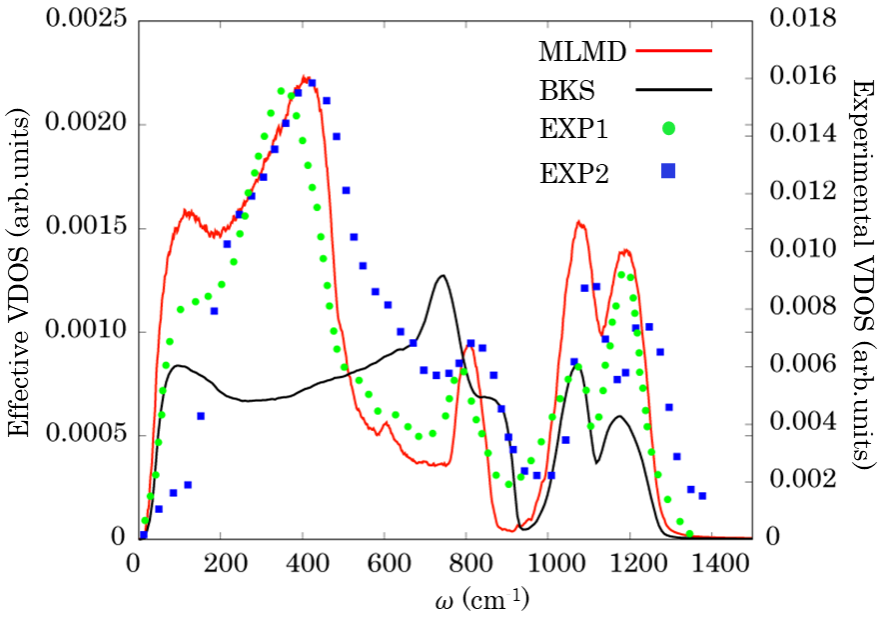

Figure S16 | Comparison between calculated and inelastic neutron scattering (INS) vibrational density of states (VDOS). The red line shows the neutron-weighted effective VDOS calculated from machine-learning MD simulations for PG/noLH (pristine glass). The black line represents the effective VDOS obtained from classical MD simulations using the BKS potential for pristine glass. Green circles (8) and blue squares (9) denote experimental INS data.

Fig. S16 shows the vibrational density of states (VDOS) calculated to assess the accuracy of machine-learning MD simulations in describing vibrational properties, together with experimental inelastic neutron scattering (INS) data. To enable a direct comparison with experiments, the calculated VDOS was weighted by neutron scattering lengths following the procedure described in Ref. (10). In addition, the results are compared with those obtained from classical molecular dynamics simulations using the widely employed BKS potential (11). Although the INS VDOS data themselves exhibit some scatter, the MLMD results successfully reproduce the major experimental features, including the positions and relative intensities of the main peaks. In contrast, classical

molecular dynamics simulations using the BKS potential show significant discrepancies from the experimental data, particularly in the frequency range of approximately 400-900 cm^{-1}, where the overall shape of the VDOS deviates markedly from that observed in INS measurements. This discrepancy indicates that conventional classical MD simulations have intrinsic limitations in capturing vibrational properties in this frequency range. As a result, it is difficult to reliably discuss variations in Raman features such as the D1 and D2 bands using standard classical force fields alone. These results demonstrate that MLMD provides a clear advantage in accurately describing vibrational properties and offers a more reliable framework for analyzing both vibrational spectra and structure–vibration relationships in silica glass. Having established that MLMD can reliably reproduce experimental vibrational features at the level of the VDOS, we now discuss how these vibrational characteristics are reflected in Raman spectra.

The Raman intensity reflects only Raman-active modes, whereas the vibrational density of states (VDOS) includes all vibrational modes. The Raman intensity $I(\omega)$ is related to the VDOS $g(\omega)$ through the Raman coupling coefficient $C(\omega)$ as

$$I(\omega) = C(\omega)\frac{n(\omega)+1}{\omega}g(\omega),$$

where $n(\omega)$ is the Bose-Einstein distribution function (12). The Raman coupling coefficient $C(\omega)$ depends not only on frequency but also on the local structure and density of the material (13). Consequently, both the intensity and position of Raman peaks are influenced by variations in $C(\omega)$, and the peaks in the VDOS do not necessarily coincide with the Raman peaks. However, qualitative trends in peak intensity and position can still be compared. Here, we focus on the changes in the D1 and D2 bands, which serve as indicators of structural changes in the Si–O network related to four- and three-membered rings. To extract the contributions of the four- and three-membered rings to the VDOS, we define the four- and three-membered VDOS as

$$g_{3(4)}(\omega) = \sum_{i\in 3(4)-\mathrm{ring}} g_i(\omega)$$

where the summation is taken only over the atoms forming the three- or four-membered rings.

Fig. S17 shows the Raman spectra and the simulated VDOS. The calculated peak positions of the D1 and D2 bands in the VDOS are reasonably close to those observed in the Raman spectra. The D1 and D2 bands of HDG shift to higher frequencies relative to PG, which is consistent with the experimental trend. The relative intensities of the D1 and D2 bands between PG and HDG, however, do not match between the VDOS and the Raman spectra. Nevertheless, there are aspects that resemble the changes observed in the Raman intensities after FLDW. The intensity of the D1 peak in PG and the D2 peaks in both PG and HDG increase upon local heating, showing a similar trend to that observed in the FLDW treated samples. In contrast, the intensity of the D1 peak in HDG does not increase by local heating, but becomes more well-defined, resembling the peak evolution observed in HPHT followed by FLDW. Although complete agreement between the Raman spectra and the calculated VDOS cannot be expected, the VDOS reproduces the experimental trends in the evolution of the D1 and D2 bands. This suggests that the simulations capture local structural changes similar to those occurring in the experiments.

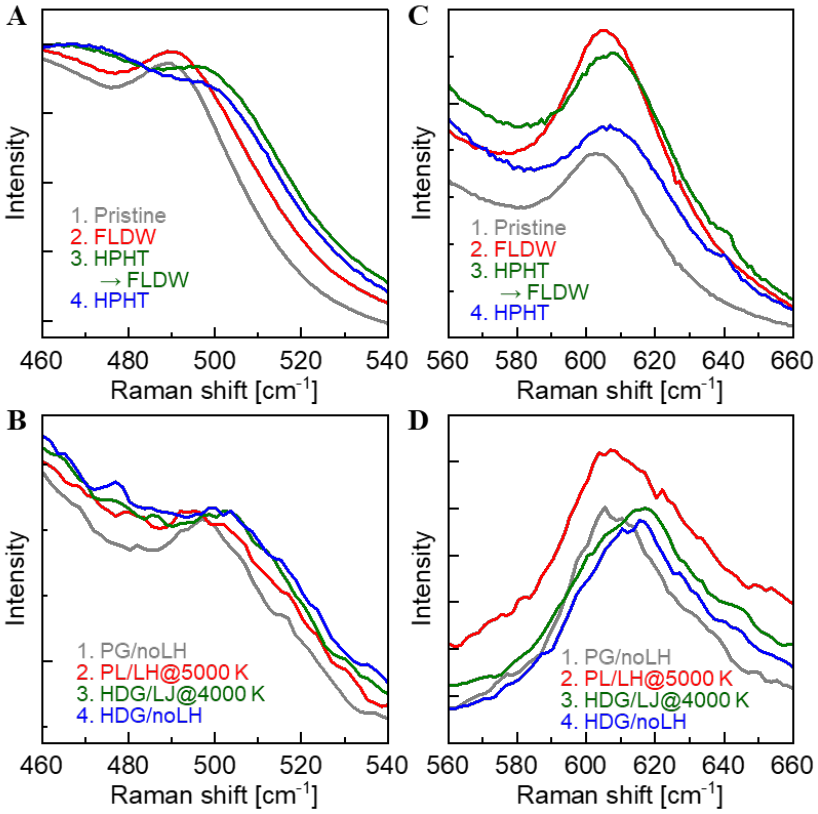

Figure S17 | Experimental Raman spectra (magnified view of Fig. 4A) and vibrational density of states (VDOS) calculated by machine-learning MD simulations. (**A**, **C**) Experimental Raman spectra showing the (**A**) D1 and (**C**) D2 bands, corresponding to four- and three-membered rings, respectively. Sample numbers: 1. Pristine glass, 2. FLDW glass (1.2 μJ), 3. HPHT glass (4.9 GPa), 4. HPHT (4.9 GPa) followed by FLDW (1.2 μJ). (**B**, **D**) Simulated VDOS of the (**B**) D1 and (**D**) D2 bands. Simulated structures: 1. PG/noLH, 2. PG/LH@5000 K, 3. HDG/LH@4000 K, and 4. HDG/noLH.

10. Crystallization of silica glass under high-pressure/high-temperature conditions

Fig. S18 presents confocal Raman spectra of silica glass subjected to HPHT treatment at 4.9 GPa and various temperatures. The appearance of characteristic coesite peaks unambiguously indicates crystallization at 823 K.

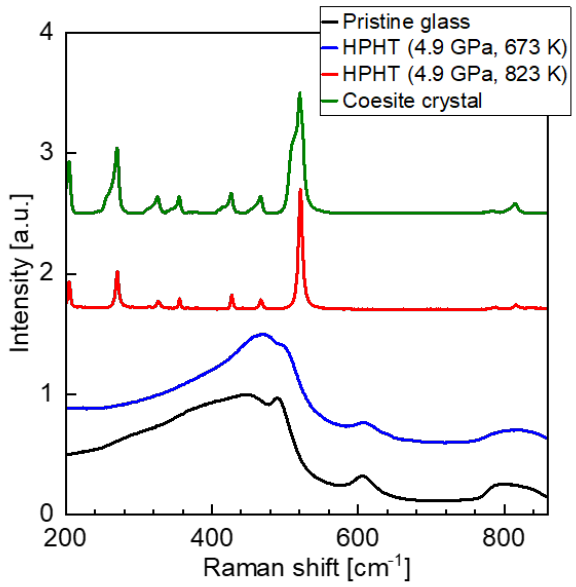

Figure S18 | Crystallization of silica glass under HPHT conditions. Confocal Raman spectra of silica glass subjected to HPHT treatment at 4.9 GPa and various temperatures. The reference Raman spectrum of a coesite crystal is also shown for comparison.

11. Calibration curve for applied pressure in high-pressure/high-temperature experiments

Fig. S19 presents calibration curve for applied pressure in HPHT experiments. The pressure calibration curve was obtained using the equation of state of MgO, based on established literature procedures (12).

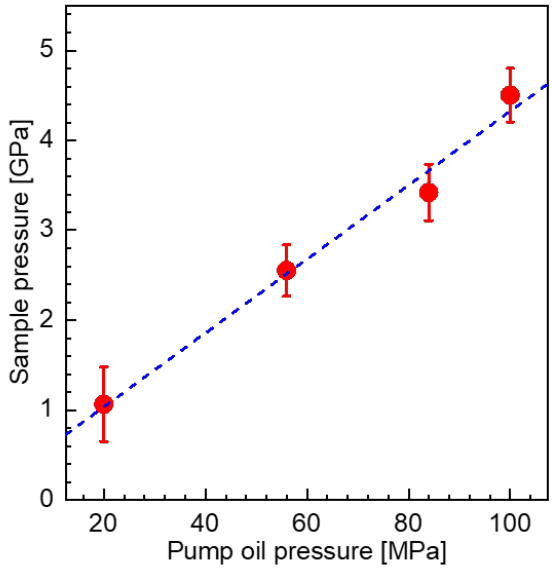

Figure S19 | Calibration curve for applied pressure. Calibration curve between the applied pressures using a hydraulic pump and the actual pressure applied to the sample.

12. Local temperature evolution during femtosecond laser irradiation

Local temperature evolution immediately after a single pulse irradiation (Fig. S20) and heat accumulation due to repetitive irradiation (Fig. S21) during femtosecond laser irradiation in silica glass were simulated using a thermal diffusion model (13).

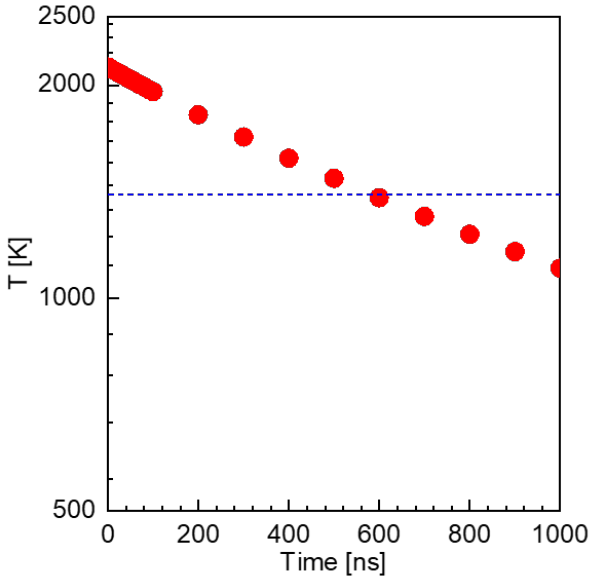

Figure S20 | Simulated temperature profile near the laser focal spot immediately after a single laser pulse irradiation. The dashed blue line indicates the glass transition temperature of silica glass.

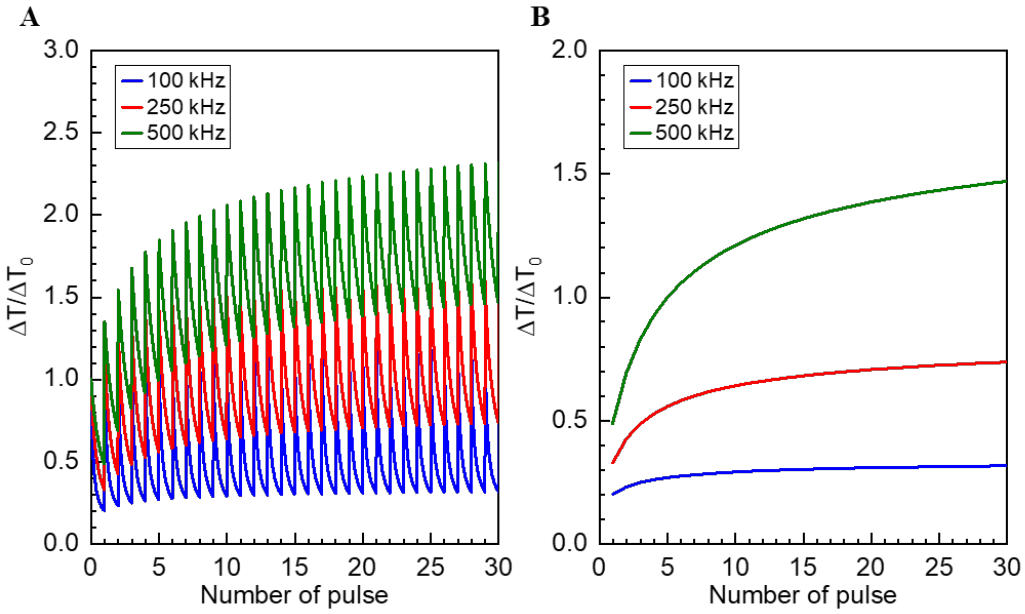

Figure S21 | Simulated temperature change during laser irradiation in silica glass. (**A**) Simulated temperature change as a function of the number of pulses at 100 kHz, 250 kHz, and 500 kHz. (**B**) Calculated temperature profile just before each shot.

Supplementary References

1. C. Martinet, V. Martinez, C. Coussa, B. Champagnon, M. Tomozawa, Radial distribution of the fictive temperature in pure silica optical fibers by micro-Raman spectroscopy. *J. Appl. Phys.* 103, 083506 (2008).
2. M. Bergler, K. Cvecek, F. Werr, M. Brehl, D. De Ligny, M. Schmidt, Cooling rate calibration and mapping of ultra-short pulsed laser modifications in fused silica by Raman and Brillouin spectroscopy. *Int. J. Extreme Manuf.* 2, 035001 (2020).
3. C. Tan, L. Zhao, M. Chen, J. Cheng, H. Yang, Q. Liu, Z. Yin, W. Ding, Morphology evolution mechanisms and localized structural modification of repaired sites on fused silica optics processed by CO_2 laser rapid ablation mitigation. *Opt. Laser Technol.* 147, 107648 (2022).
4. T. Zhang, L. Zhao, J. Cheng, Z. Yin, T. Li, M. Chen, W. Liao, X. Yuan, Role of fictive temperature distribution involved in CO_2 laser polishing of fused silica and its optimization for achieving even heat-affected zones. *Appl. Surf. Sci.* 670, 160605 (2024).
5. K. Saito, A.J. Ikushima, Structural relaxation enhanced by impurities in silica glass. *AIP Conf. Proc.* 469, 507-512 (1999).
6. S. Plimpton, Fast parallel algorithms for short-range molecular dynamics. *J. Comput. Phys.* 117, 1-19 (1995).
7. K. Kobayashi, Y. Nagai, M. Itakura, M. Shiga, Self-learning hybrid Monte Carlo method for isothermal-isobaric ensemble: Application to liquid silica. *J. Chem. Phys.* 155, 034106 (2021).
8. F.L. Galeener, A.J. Leadbetter, M.W. Stringfellow, Comparison of the neutron, Raman, and infrared vibrational spectra of vitreous SiO_2, GeO_2, and BeF_2. *Phys. Rev. B* 27, 1052 (1983).
9. M.J. Carpenter, D.L. Price, Correlated motions in glasses studied by coherent inelastic neutron scattering. *Phys. Rev. Lett.* 54, 441 (1985).
10. S. N. Taraskin and S. R. Elliott, Connection between the true vibrational density of states and that derived from inelastic neutron scattering, *Phys. Rev. B* 55, 117 (1997).
11. B. W. H. van Beest, G. J. Kramer, and R. A. van Santen, Force fields for silicas and aluminophosphates based on ab initio calculations. *Phys. Rev. Lett.* 64, 1955 (1990).
12. Y. Kono, T. Irifune, Y. Higo, T. Inoue, A. Barnhoorn, P-V-T relation of MgO derived by simultaneous elastic wave velocity and in situ X-ray measurements: A new pressure scale for the mantle transition region. *Phys. Earth Planet. Inter.* 183, 196-211 (2010).
13. M. Shimizu, M. Sakakura, M. Ohnishi, Y. Shimotsuma, T. Nakaya, K. Miura, K. Hirao, Mechanism of heat-modification inside a glass after irradiation with high-repetition rate femtosecond laser pulses. *J. Appl. Phys.* 108, 073533 (2010).